Understanding methanol dissociative adsorption and oxidation on amorphous oxide films

Journal:	*Faraday Discussions*
Manuscript ID	FD-ART-11-2021-000109.R1
Article Type:	Paper
Date Submitted by the Author:	12-Dec-2021
Complete List of Authors:	Padavala, Sri Krishna Murthy; Oregon State University, School of Chemical, Biological, and Environmental Engineering Artyushkova, Kateryna; Physical Electronics Inc Boettcher, Shannon; University of Oregon, Department of Chemistry & Biochemistry and the Materials Science Institute Nemšák, Slavomír; Lawrence Berkeley National Laboratory, Advanced Light Source Stoerzinger, Kelsey; Oregon State University, School of Chemical, Biological, and Environmental Engineering; Pacific Northwest National Laboratory, Physical and Computational Sciences Directorate

1. Title

Understanding methanol dissociative adsorption and oxidation on amorphous oxide films

2. Authors

Sri Krishna Murthy Padavala,[1] Kateryna Artyushkova,[2] Shannon W. Boettcher,[3] Slavomir Nemsak,[4] Kelsey A. Stoerzinger[1,5,*]

[1]School of Chemical, Biological and Environmental Engineering, Oregon State University, Corvallis, Oregon 97331, USA

[2]Physical Electronics Inc. Chanhassen MN, 55317 USA

[3]Department of Chemistry & Biochemistry and the Materials Science Institute, University of Oregon, Eugene, Oregon 97403, USA

[4]Advanced Light Source, Lawrence Berkeley National Laboratory, 1 Cyclotron Road, Berkeley, CA 94720, USA

[5]Physical and Computational Sciences Directorate, Pacific Northwest National Laboratory, Richland, Washington 99354, USA

*kelsey.stoerzinger@oregonstate.edu

3. Abstract

Interactions between a transition metal (oxide) catalyst and a support can tailor the number and nature of active sites, for instance in the methanol oxidation reaction. We here use ambient pressure X-ray photoelectron spectroscopy (AP-XPS) to identify and compare the surface

adsorbates that form on amorphous metal oxide films that maximize such interactions. Considering $Al_{(1-x)}M_xO_y$ (M=Fe or Mn) films at a range of methanol:oxygen gas ratios and temperatures, we find that the redox-active transition metal site (characterized by methoxy formation) dominates dissociative methanol adsorption, while basic oxygen sites (characterized by carbonate formation) play a lesser role. Product detection, however, indicates complete oxidation to carbon dioxide and water with partial oxidation products (dimethyl ether) comprising a minor species. Comparing the intensity of methoxy and hydroxyl features at a fixed XPS chemical shift suggests methanol deprotonation during adsorption in oxygen rich conditions for high transition metal content. However, increasing methanol partial pressure and lower metal site density may promote oxygen vacancy formation and the dehydroxylation pathway, supported by a nominal reduction in the oxidation state of iron sites. These findings illustrate that AP-XPS and mass spectrometry together are powerful tools in understanding metal-support interactions, quantifying and probing the nature of catalytic active sites, and considering the link between electronic structure of materials and their catalytic activity.

4. Introduction

Methanol (CH_3OH) is a versatile and flexible chemical that can be used both as a fuel source and chemical feedstock[1, 2]. CH_3OH oxidation involves a series of oxidation and dehydration reactions[3] with numerous potential products depending on the reaction pathway. For example, partial oxidation of CH_3OH can yield formaldehyde (CH_2O), dehydration and C-O coupling produces dimethyl ether $(CH_3)_2O$, and complete oxidation yields water (H_2O) and carbon dioxide (CO_2). The methanol oxidation reaction (MOR) can be used as a probe to quantify the density of active sites on oxide surfaces[4, 5], and due to its diverse potential products

and pathways, help ascertain the nature of these active sites[4]. Considering a broad range of metal oxides, CH_2O is formed on redox-active sites, $(CH_3)_2O$ is formed on Brønsted acid sites, and CO_2 is formed on basic sites[4].

The MOR has been studied on transition metals (e.g. V, Cu, Mn, Fe, Mo, Pd, Au) and their oxides with and without supports[6-13]. Supports not only disperse the catalyst as small particles with high surface area, but also can modify the activity of the catalyst and influence its selectivity towards the different products of MOR. Considering the common support material of γ-alumina, previous reports have shown that this material alone will oxidize CH_3OH to $(CH_3)_2O$ in oxygen rich environments at temperatures <275 ℃, above which carbon monoxide (CO) begins to form. By incorporating manganese and iron oxide catalysts onto γ-alumina supports, $(CH_3)_2O$ remained the primary oxidation product but formed at lower temperatures, and above 200 ℃ complete oxidation to CO_2 dominated[14]. As oxide supports can carry their own activity towards MOR, the activity of and product distribution from supported catalysts thus depends on the catalyst loading.[9]

In order to maximize effects localized to the catalyst-support interface, the interface density can be increased by dispersion of small catalyst nanoparticles. The extension of this is the incorporation of transition metals into a support host directly, thus maximizing electronic interactions and potential dual-active site effects. Herein, we prepare amorphous metal oxides (AMOs) by embedding the transition metal ion into the support, resulting in uniform interaction between “support” and “catalyst” metal centers over the surface of AMOs. Such AMOs find use in many fields ranging from electronics to heterogeneous catalysis[15-17]. The electronic structure of these materials can be tailored for a given application, influencing for example their corrosion-resistance properties[18] and electrochemical activity[19].

Alumina's acid/base characteristics, which maximize dispersion of transition metal (oxides) on supports, facilitate the incorporation of a wide range of transition metal cations at high concentrations in AMOs[17]. The addition of iron (Fe) and manganese (Mn), here model catalyst centers for the MOR, leads to new filled electronic states in alumina-based AMOs at the top of the valence band[20]. In our previous work, we investigated the influence of these new electronic states on the surface acidity, basicity, and the hydroxylation behavior in a humid environment[21]. In the current work, we study the influence of these new electronic states on the surface reactivity towards CH_3OH.

We have used ambient pressure X-ray photoelectron spectroscopy (AP-XPS) to investigate CH_3OH oxidation on $Al_{(1-x)}M_xO_y$ (M = Fe, Mn) AMO films across temperatures and methanol:oxygen gas ratios. For the compositions considered here, Fe and Mn are fully dispersed without evidence of phase segregation and the formation of transition metal oxide clusters[17]. The nominal oxidation state of Fe and Mn in the films is +3, and the basicity of the films increases with Fe content. Both methoxy (here referred to as OCH_3) and carbonate (here termed CO_3) species are observed on the surface, where the increase in OCH_3 coverage with increase in transition metal content suggests that transition metal sites are active for CH_3OH oxidation. The $Al_{(1-x)}Fe_xO_y$ and $Al_{(1-x)}Mn_xO_y$ oxide films studied here had fewer basic sites (characterized by CO_3 formation) compared to acidic and redox-active sites (characterized by OCH_3 formation). Consideration of OCH_3 and hydroxyl (here termed OH) features in the O 1s and C 1s core levels suggests that the chemical shift for and/or intensity of OH varies with the methanol:oxygen gas ratio and AMO composition.

5. Experimental

Thin-film preparation

Precursor solutions were prepared by mixing different ratios of 1 M aqueous solutions of transition metal nitrate salts, $Mn(NO_3)_2$ and $Fe(NO_3)_3$ and 1 M aqueous solution of $Al(NO_3)_x(OH)_{3-x}$ clusters, prepared by bulk electrolysis using a procedure from the literature and described previously[17]. The solution was spun coat onto a polished Si(100) substrate previously coated with Ti and Ir by electron-beam evaporation to mitigate charging, and annealed at 450°C for 30 min[20]. The thin films obtained were atomically smooth with a root-mean-square roughness (R_{rms}) <1 nm as determined by atomic force microscopy. The films are referred to by their metal ratios, i.e. a film with 80% Al and 20% Fe is called as Al8Fe2.

AP-XPS

AP-XPS was performed at the beamline 9.3.2 at the Advanced Light Source[22]. Films were placed atop a BN heating element on a sample holder containing no Pt, and grounded through a thermocouple pressed onto the film surface and electrically isolated from the holder with a ceramic. Films were cleaned by UV ozone prior to loading into the sample chamber, and cleaned *in-situ* by heating to 300 °C in an atmosphere of 100 - 150 mTorr of O_2. Following cleaning, films were then cooled to room temperature under 100 mTorr O_2. Films were characterized at room temperature and during a temperature ramp for 10:100, 50:100, and 100:50 mTorr methanol:oxygen gas. Figure S1 shows example survey spectra collected at 690 eV for 50 mTorr CH_3OH and 100 mTorr oxygen at 25 °C for the Al8Fe2 and Al4Fe6 films depicting the expected features. The incident photon energy was calibrated at room temperature by cross-referencing O 1s (690 eV, 750 eV) and Al 2p (490 eV, 350 eV) core levels in duplicate films previously calibrated to the Au 4f (84 eV) of an auxiliary reference[21], where the resultant O 1s and Al 2p binding energy (BE) is dependent on composition as discussed in section 6.2. Subsequent

measurements at elevated temperatures were calibrated to the Al 2p core level as an internal standard. The spectra were fit with CasaXPS using a Shirley-type background subtraction. The identified features were fit using a line shape with 70% Gaussian and 30% Lorentzian character with average fitted values shown in Table S1 and S2. The OH+OCH_3 feature in the O 1s core level was constrained at 1.65 eV above the bulk O 1s BE based on previous measurements made for duplicate films in water[21], unless stated otherwise.

6. Results and Discussion

6.1 Feature Identification

We first describe the features observed in each core level, considering the example case of 50 mTorr CH_3OH and 100 mTorr oxygen at room temperature.

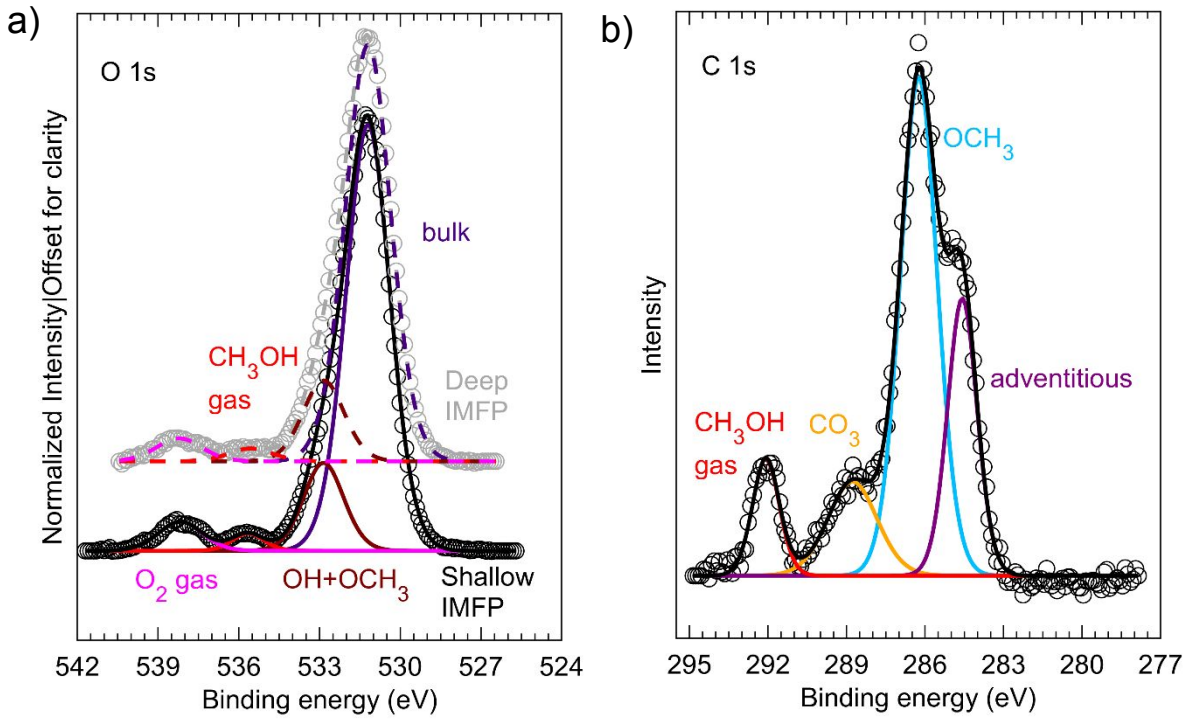

Figure 1: (a) O 1s and (b) C 1s for Al8Fe2 in 50 mTorr of CH_3OH and 100 mTorr of oxygen at a) . a) O 1s probed at an incident photon energy (IPE) of 690 eV (shallow inelastic mean free path (IMFP) ~5.8 Å[23], solid line) and 750 eV (deep IMFP ~6.6 Å[23], dashed line). Features at the surface ($OH+OCH_3$) are less intense when probed with a greater IPE. b) C 1s core level (490 eV IPE) depicting the different features observed.

O 1s core level: For the oxygen core level, four distinct features, shown in Figure 1a), were observed across all samples and conditions. Depth profiling established that the feature at ~531 eV is due to the bulk of the film, while the higher BE shoulder is due to adsorbates, with integrated intensity ratio of shoulder/bulk as 0.19 and 0.18 in Figure 1 probed at 690 eV (shallow inelastic mean free path (IMFP) ~5.8 Å[23]) and 750 eV (deep IMFP ~6.6 Å[23]) incident photon energy (IPE). This shoulder at 1.65 eV above the bulk is attributed in part to OH species based on previous measurements of duplicate samples in water[21]. Any oxidized carbon species on the surface will also have similar O 1s BEs, and are primarily attributed to OCH_3 species based on the C 1s spectra (Figure 1b). The relative sensitivity factor (RSF) for O 1s (690 eV) to the C 1s (490 eV) was determined to be 1.08 by measuring gaseous CO_2. The features at ~535 eV[6] and ~538 eV[6] are attributed to gas phase CH_3OH and oxygen, respectively, with their relative intensities consistent with gas-phase partial pressures and experimentally measured O:C RSF. Table S1 shows the average BEs and the full width half maximum (FWHM) of the features observed in the oxygen core level for the films across different methanol:oxygen gas ratios at different temperatures. Example room temperature oxygen core level spectra in Figure S2 depict the changes in feature BE and intensity with film composition and gas ratio.

C 1s core level: For the carbon core level, four distinct features at ~284.8 eV, ~286.1 eV, ~

288.6 eV and ~292 eV were observed as shown in Figure 1 b). The feature at ~284.8 eV is adventitious carbon (CH_x)[24]. The feature at 286.1 eV is at BE consistent with C-O or C≡O bonds, potentially from a OCH_3 species or CO[25]. Although both can be intermediates in MOR, we assign this feature to OCH_3 as it is the predominant intermediate for the MOR on transition metals[4, 7, 26]. The feature at 288.6 eV arises from CO_3[27] and the feature at 292 eV from gas phase CH_3OH. A small amount of K was observed on the Al4Fe6 sample (Figure S3); based on tabulated cross sections, the abundance of K is ~10x lower than its 2p intensity ratio with C 1s at 490 eV. Table S2 shows the average BE and FWHM of the features observed in the carbon core level for the films across different methanol:oxygen gas ratios at different temperatures. Example room temperature carbon core level spectra in Figure S2 depict the changes in feature BE and intensity with film composition and gas ratio.

Metal core levels: For Al8Fe2, four distinct features at ~74 eV, ~62 eV, ~66 eV and ~56 eV were observed as shown in Figure S4. The feature at ~74 eV is assigned to the Al 2p core level and that at ~56 eV to the Fe 3p core level, whose BE is referred to here as that from a single Gaussian-Lorentzian feature. The features at ~62 eV and ~66 eV are assigned to the Ir 4f doublet from the conductive substrate coating. Comparing across IPEs with varied mean free paths, the Ir layer remains buried under the $Al_{(1-x)}M_xO_y$ film (Figure S5). A similar spectrum was obtained for the Al4Fe6 film as well. For the sample with Mn content, a feature at ~47 eV was observed (Figure S4) instead of ~56 eV, which is assigned to the Mn 3p.

6.2 Electronic structure of the amorphous oxide films

We first consider the electronic structure of the Al8Fe2, Al4Fe6, and Al6Mn4 films by comparing their metal and oxygen core levels, as well as the valence band (VB). In all films,

173 fitting of the Fe 3p and Mn 3p (Figure S6-7) core levels gives a nominal oxidation state of +3[20].
174 The oxidation state of the Fe 3p can be assessed using its FWHM (Figure S7) and BE (discussed
175 in detail in section 6.3.4). While the oxidation state of Fe 3p is predominantly +3 for the different
176 gas compositions and temperatures, small changes in oxidation state with gas composition and in
177 some cases temperature (consistent with VB spectra as shown in Figure S8) for Fe-containing
178 films are discussed in more detail in section 6.3.4. The VB edge, fit with a step down function
179 and noted at half height, is highest in BE—furthest from the Fermi level—for Al8Fe2 (Table 1
180 and Figure S9), but shifts approximately ~1 eV lower with increasing Fe content in Al4Fe6, and
181 is similar for Al6Mn4. For other methanol:oxygen gas ratios, the VB edge is similar for Al8Fe2
182 and Al6Mn4, but decreases with increase in Fe content in Al4Fe6 (Figure S9). The use of a
183 conductive Ir underlayer beneath the 5 nm AMO film, grounding of the AMO film surface
184 through the thermocouple, and presence of gas phase photoelectrons mitigate potential charging
185 effects. For example, the as measured BE of the bulk O 1s (750 and 690 eV IPE) and Al 2p (690,
186 490, and 350 eV IPE) of Al8Fe2 in 10:100 mTorr methanol:oxygen decreased only ~0.2 eV
187 upon heating from room temperature to 275 °C, suggesting minimal potential charging effects.

Core level	BE for Al8Fe2 (eV)	BE for Al4Fe6 (eV)	BE for Al6Mn4 (eV)
O 1s (bulk)	531.4	530.9	531.2
Al 2p	74.2	74	74.3
M 3p	56.1	55.7	48.8
VB edge	3.7	2.7	2.5

188 Table 1: BE of the bulk O 1s, Al 2p, M 3p and VB edge for Al8Fe2, Al4Fe6 and Al6Mn4 films
189 for 50 mTorr of CH_3OH and 100 mTorr of oxygen at 25 °C.

Similarly, both the bulk O 1s feature and the Fe 3p shift to ~0.5 eV and ~0.4 eV lower BE with increasing Fe content (Figure S9). This could include effects from a shift in the rigid electronic structure (lesser charging) with Fe substitution, given the shift of VB edge towards the Fermi level, however we note that at the same IPE, the VB edge shifts by 1 eV while the Al 2p shifts by only 0.2 eV. Thus, a lower bulk O 1s BE may also indicate a greater basicity (electron density) on O, though surprising given the more covalent nature of Fe-O versus Al-O bonds based on electronegativity differences. In addition, the bulk O 1s feature shifts to lower BE for more reducing methanol:oxygen gas ratios with increasing temperature (Figure S10).

6.3 Adsorbate formation and mechanistic implications

We next consider the surface speciation and its relation to AMO composition and electronic structure. On oxides, CH_3OH dissociatively adsorbs to form CH_3O groups either by deprotonation at a metal site or dehydroxylation at an oxygen site. The metal site (*M*) is considered redox-active (*O* + *M* + CH_3OH → CH_3O-*M* + H-*O*), whereas a surface *O*-H group can give up a proton (acidic character) to dehydrate CH_3OH in this process (H-*O* + CH_3OH → CH_3-*O* + H_2O)[4]. OCH_3 groups can subsequently deprotonate to form CH_2O, or C-O coupling can occur between a CH_3 group and CH_3O-*M* to form $(CH_3)_2O$. Adsorbed CO_3 is expected to form at basic sites as a precursor to CO_2 desorption (O_2C-*O* → *O* + CO_2). We consider the relative abundance of OCH_3 and CO_3 surface species as obtained by the fitting of the C 1s spectra for different methanol:oxygen gas ratios (noted in mTorr) and temperature to understand the nature of AMO active sites for MOR.

6.3.1 Formation of adsorbates across compositions and conditions

Changes in film composition can affect the formation of OCH_3 groups. The intensity of the OCH_3 (C 1s) normalized to that of the bulk oxide (O 1s) is compared across Fe-containing samples (Figure 2). If the intensity of bulk O is not attenuated appreciably by other species, such as adventitious carbon, this ratio is proportional to elemental coverage[28]. As expected with an increase in thermal energy, the OCH_3/bulk ratio decreases with increase in temperature. We note, however that the steeper decrease for Al4Fe6 for temperatures > 150 ℃ is commensurate with observed conversion to CO_2 and H_2O (Figure S11). The OCH_3 coverage is greater for Al4Fe6 compared to Al8Fe2 for all methanol:oxygen gas ratios, indicating that Fe is active for OCH_3 formation. While the OCH_3/bulk ratio at room temperature increases with the partial pressure of CH_3OH in the chamber, indicating sub-monolayer concentration on the surface, this increase is smallest on Al8Fe2 (and negligible comparing 50:100 and 100:50 methanol:oxygen gas ratios), further confirming the role of Fe in OCH_3 formation. The drop in OCH_3/bulk ratio with increasing temperature is larger for Al4Fe6 (77% for 50:100 methanol:oxygen gas ratio) than Al8Fe2 (46%) which may indicate that while substitution of more acidic Fe for Al increases the number of sites for OCH_3 formation, it also reduces the strength of their binding or facilitates their oxidative removal.

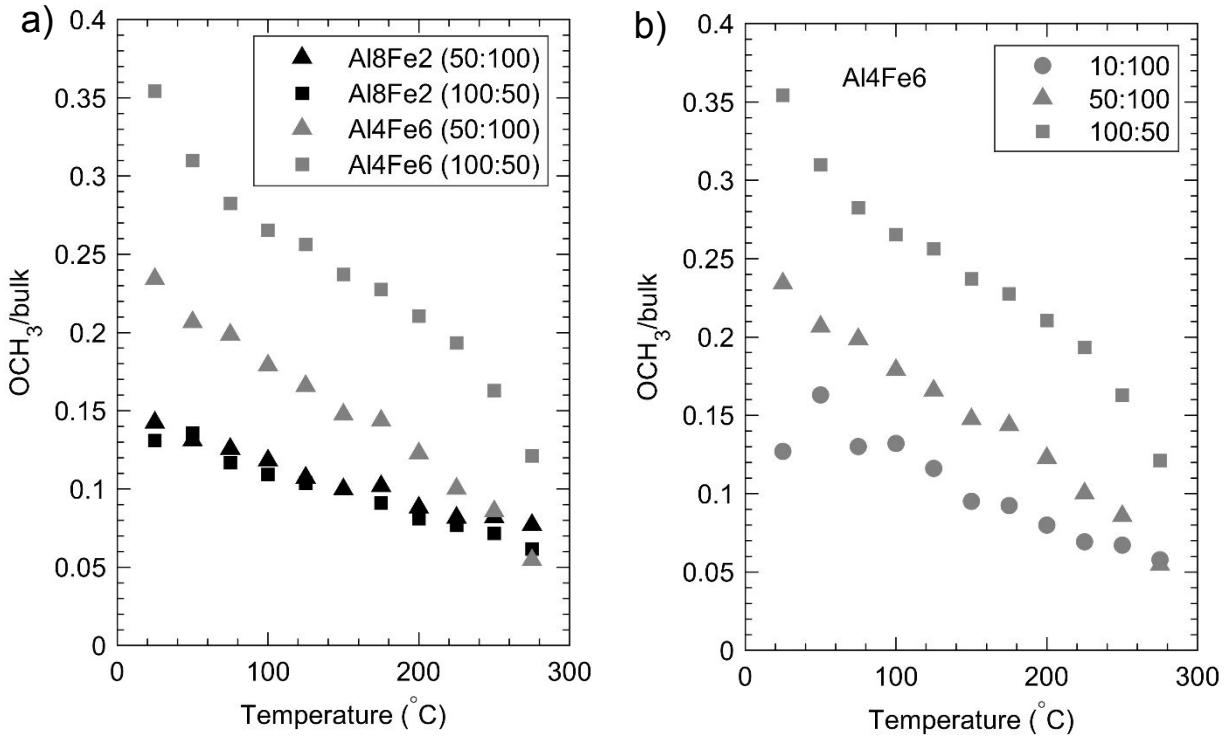

Figure 2: Ratio of OCH_3 (C1s) to the bulk (O1s) with temperature for a) Al8Fe2 and Al4Fe6 for 50:100 and 100:50 methanol:oxygen gas ratios and b) Al4Fe6 for different gas ratios, where the OCH_3 coverage increases with CH_3OH partial pressure in the reactant gas. In the above figure, 10:100, 50:100 and 100:50 denote the pressures of methanol:oxygen in mTorr.

To assess the coverage of CO_3 (expected at basic sites as a precursor to CO_2 desorption), its intensity is calculated relative to the bulk. The CO_3/bulk ratio is comparable on both Fe-containing films (Figure 3 and Figure S12). The shift in bulk O 1s to lower BE from Al8Fe2 to Al4Fe6 is consistent with an increase in basicity of the O^{2-} sites upon incorporation of Fe^{3+} into the Al^{3+}-oxide host (Table 1, Figure S9). The comparable CO_3/bulk ratio for these two films may thus suggest basic sites are not the primary contributor to CH_3OH oxidation under these

conditions, assessed more in the following section. The CO_3/bulk ratio decreases with temperature for all film compositions (Figure S12). Generally, the amount of CO_3 on the surface also decreases with decreasing partial pressure of oxygen as shown in Figure 3, as would be expected given its production from complete CH_3OH oxidation at a stoichiometric 3:2 methanol:oxygen ratio. A notable exception is Al4Fe6 in 100:50 mTorr methanol:oxygen, which has greater CO_3 coverage compared to 50:100 mTorr methanol:oxygen.

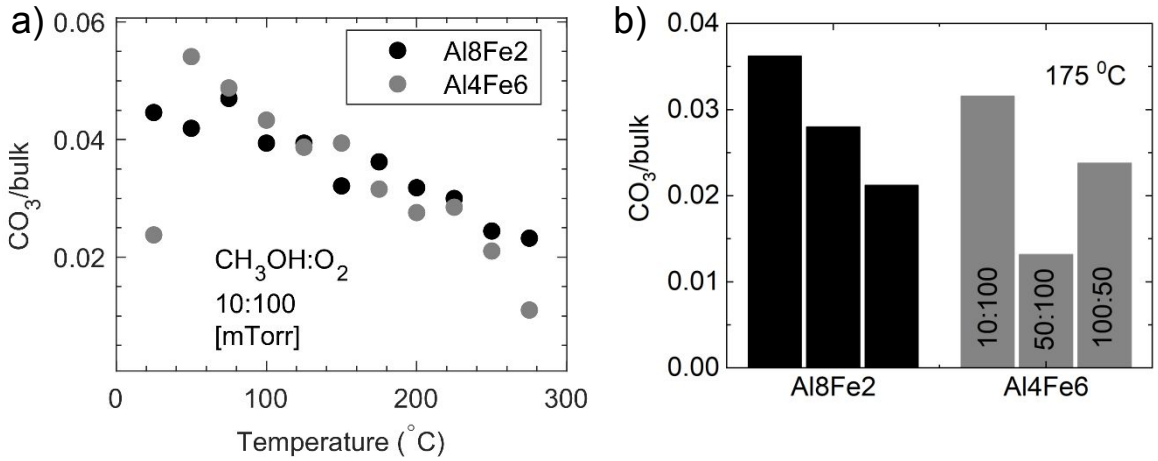

Figure 3: Ratio of the CO_3 (C1s) to bulk (O1s) for a) Al8Fe2 and Al4Fe6 for 10 mTorr of CH_3OH and 100 mTorr of oxygen with temperature and b) Al8Fe2 and Al4Fe6 at 175 ℃ for noted methanol:oxygen gas pressures [mTorr].

6.3.2 Nature of active site

To better understand the nature of the active site and pathway for CH_3OH oxidation, we consider the relative coverage of CO_3 and OCH_3 species (Figure 4). The CO_3/OCH_3 ratio is similar (0.3-0.4) across films in 10:100 mTorr of methanol:oxygen.

The CO_3/OCH_3 ratio tells the ratio of the number of basic (CO_3 forming) to acidic and redox-active (OCH_3 forming) sites. For all films considered here, the number of basic sites is more than two times lower than the total number of acidic and redox-active sites. The CO_3/OCH_3 ratio decreases with increase in CH_3OH partial pressure indicating that the formation of CO_3 (completely oxidized product) decreases as oxygen partial pressure is decreased, also evident from considering the CO_3/bulk oxide ratio (Figure 3, S12). For amorphous Al4Fe6, we observe complete oxidation products of CO_2 and H_2O with a mass spectrometer for both 10:100 and 50:100 methanol:oxygen ratios (Figure S10) starting at 150 ℃, but not $(CH_3)_2O$ at any temperatures. For amorphous Al6Mn4 in 50:100 methanol:oxygen, CO_2 and H_2O are produced starting at 200 ℃, with small amounts of $(CH_3)_2O$ at lower temperatures (Figure S11), although we note that the quantification of evolved gases in the spectrometer is not calibrated. More notable complete oxidation products on Al4Fe6, compared to Al6Mn4, is consistent with both the lower CO_3/OCH_3 ratio (Figure 4) and the concurrent greater reduction in adsorbed OCH_3 as temperature is increased (Figure 2).

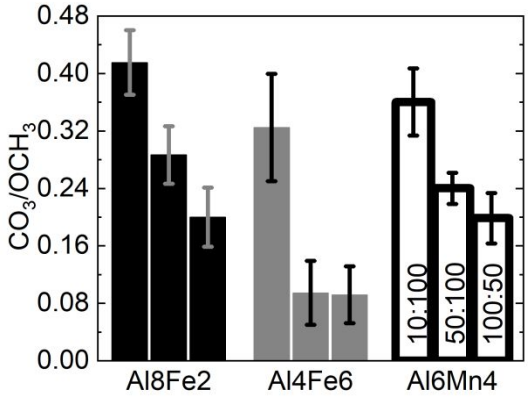

Figure 4: Average ratio of CO_3 (C 1s) to OCH_3 (C1s) species taken across temperatures for the Al8Fe2, Al4Fe6 and Al6Mn4 films. The relative abundance of CO_3 decreases with increasing the CH_3OH partial pressure in the reactant gas. In the above figure, 10:100, 50:100 and 100:50 denote the pressure of methanol:oxygen in mTorr.

6.3.3 Mode of methanol dissociation on the films

We next examine the intensity ratio of the OCH_3 and OH features to ascertain the mode of CH_3OH activation on the surface. In the O 1s, these features cannot be distinguished and are fit as a single peak. In the C 1s, a distinct OCH_3 feature is fit. As the experimentally measured RSF of O:C is close to 1, taking the ratio of the OH+OCH_3 feature in the O 1s (fit at a chemical shift of 1.65 eV from the bulk) to the OCH_3 feature in the C 1s (approximately 1.6 eV relative to adventitious carbon), here referred to as the O:C ratio (Figure 5), readily approximates the abundance ratio of these adsorbates, provided they are observable at the fit chemical shift. We note that the lower abundance of CO_3 on the surface, which is similar across samples and conditions, is not fit in the O 1s and would result in a roughly consistent offset to this ratio. CH_3OH has been previously proposed[5] to adsorb dissociatively by forming surface OCH_3 groups with the oxygen atom bonding to the metal site (CH_3O-*M*) and the proton from the alcoholic group bonding to a nearby lattice oxygen site forming *O*-H on the surface. An O:C ratio greater than 1 is consistent with both OCH_3 and OH groups giving rise to distinct XPS chemical shifts in the O 1s. The reduction in O:C ratio with increasing CH_3OH partial pressure for Al4Fe6 suggests some O species may not give rise to distinct chemical shifts (or a smaller shift poorly fit in the fixed binding energy offset employed here), or the removal of OH groups (probably as H_2O) from the surface, with lattice oxygen replenished by O_2 gas. The value of the fit O:C ratio is

greater when the BE of the O 1s OH+OCH_3 feature floats freely, however the ratio for Al4Fe6 remains higher than that for Al8Fe2 at low CH_3OH partial pressure and comparable under reducing conditions (Figure S13). Al8Fe2 maintains comparable O:C ratio with CH_3OH partial pressure, however the Al6Mn4 O:C ratio decreases with increase in methanol partial pressure, just as for Al4Fe6, with relaxed fit.

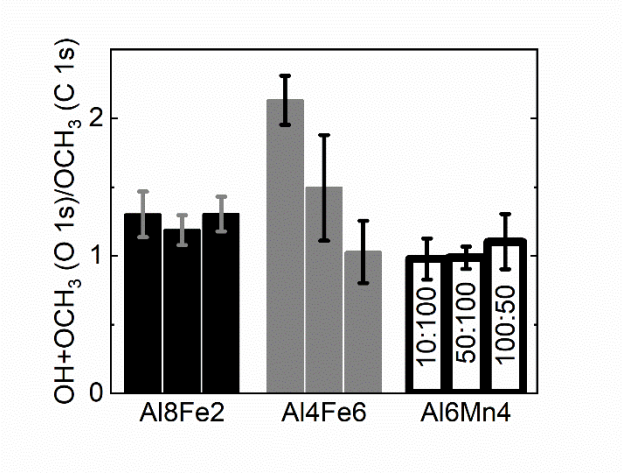

Figure 5: Average across temperatures for the ratio of OH+OCH_3 feature (O 1s) to OCH_3 feature (C 1s) for different methanol:oxygen gas pressures for the Al8Fe2, Al4Fe6 and Al6Mn4 films. In the above figure, 10:100, 50:100 and 100:50 denote the pressure of methanol:oxygen in mTorr.

The higher O:C ratio for Al4Fe6 at low CH_3OH pressures may indicate that the increased basicity of O sites upon Fe incorporation result in robust O 1s XPS chemical shifts at low OCH_3 coverage but less so as Fe sites become saturated. This is consistent with Al8Fe2, with constant OCH_3 coverage indicating site saturation, having a low O:C ratio regardless of CH_3OH partial pressure.

6.3.4 Changes in Fe electronic structure

To further assess the role of transition metal in activating CH_3OH, we consider potential changes in Fe valence. The BE of Fe 3p remains similar with temperature but decreases with increase in CH_3OH partial pressure in the reactant gas (Figure 6 and Figure S9). Considering the negligible change in OCH_3 coverage with increase in partial pressure of CH_3OH for Al8Fe2, suggesting saturation of active sites, this decrease may result from the formation of oxygen vacancies under more reducing conditions. Oxygen vacancies may similarly contribute to the observed Fe 3p shift to lower BE in Al4Fe6, however the increase in OCH_3 coverage on Al4Fe6 with CH_3OH pressure might also result in Fe reduction. In contrast to other conditions, the Fe 3p BE of Al8Fe2 in a 100:50 methanol:oxygen gas ratio decreases with increasing temperature, commensurate with a new feature below the VB edge consistent with the presence of Fe^{2+} (Figure S8). Observable reduction of Fe in Al8Fe2, but not Al4Fe6, might arise from a larger proportion of the Fe sites (presumed saturated with OCH_3 species on Al8Fe2) driving CH_3OH (partial) oxidation with increasing temperature.

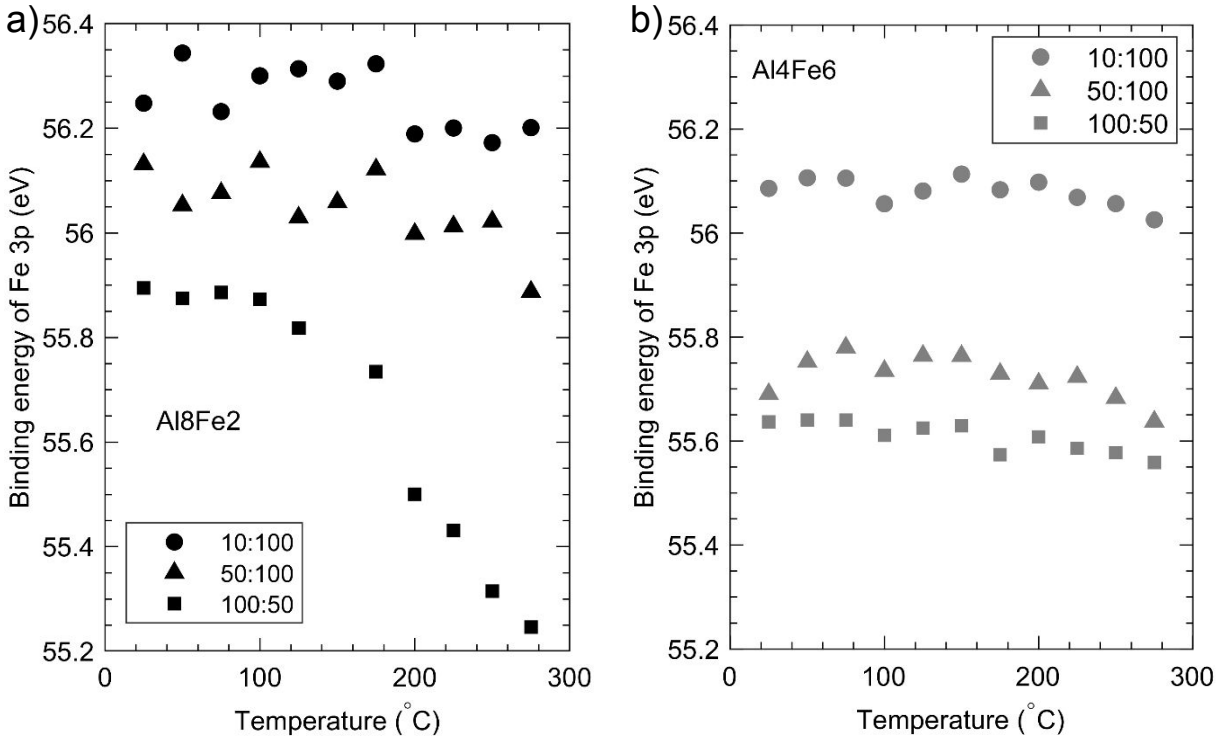

Figure 6: BE of Fe 3p with temperature for a) Al8Fe2 and b) Al4Fe6 for different methanol:oxygen gas ratios. In the above figure, 10:100, 50:100 and 100:50 denote the pressure of methanol:oxygen in mTorr.

7. Discussion

In this study, we have incorporated transition metals (Fe, Mn) into an amorphous Al oxide host as a model of highly dispersed catalyst/support for the MOR. Cations with d^5 (Fe^{3+}) and d^4 (Mn^{3+}) electronic configuration add new electronic states at top of the VB edge and within the bandgap of alumina[17, 20]. Further, the average coordination number of the Fe^{3+} and Mn^{3+} in the films considered is similar to that of alumina, ~4.5, indicating dispersed substitution for Al within the amorphous host without phase segregation. In these films, the interaction between "catalyst" (Fe, Mn ions) and "support" (Al oxide) is extended uniformly across the surface, as

evidenced by the shift in VB maximum and bulk oxygen BE towards the Fermi level with Fe content (Figure S7). However, this increase in oxygen basicity did not translate to increased coverage of CO_3 on the surface under MOR conditions, suggesting that oxygen sites do not dominate CH_3OH activation. With low metal content, the coverage of OCH_3 was independent of CH_3OH partial pressure, suggesting saturation of active sites. In contrast, OCH_3 coverage increased with CH_3OH partial pressure at higher metal content, consistent with CH_3OH activation primarily occurring at these redox-active sites whose oxidation state lowered with OCH_3 adsorption.

Previous reports have incorporated manganese and iron oxide catalysts onto γ-alumina supports, which lowered the temperature of MOR compared to the support alone in an approximately 10:100 methanol:oxygen ratio[14]. At low temperatures, $(CH_3)_2O$ was the primary oxidation product, while complete oxidation to CO_2 dominated above 200 ℃. For AMO films, despite the greater coverage of OCH_3 compared to CO_3 species, little to no $(CH_3)_2O$ is observed on Al4Fe6, with small amounts forming at temperatures as low as ~50 °C on Al6Mn4. Formation of $(CH_3)_2O$ requires C-O coupling between two adjacent $(O)CH_3$ groups, which may be limited by the dispersion of active transition metal sites in the solid-substitution amorphous films considered here. In contrast, complete oxidation to CO_2 and H_2O is observed at 150 ℃—lower in AMOs than discrete supported catalysts by 50 ℃—indicating that dispersing metal sites in amorphous oxide hosts is a promising route to maximize support effects in MOR.

8. Conclusions

We have employed AP-XPS to study the role of transition metal and its concentration on the dissociative adsorption and oxidation of methanol on amorphous $Al_xM_{(1-x)}O_y$ films, where M=Fe or Mn. Alumina's acid/base characteristics, which maximize dispersion of transition metal (oxides) on supports, facilitate their incorporation at high concentrations in AMOs. We here find that this dispersion in an amorphous framework reduces the temperature of complete methanol oxidation compared to supported MO_x/Al_2O_3 systems in literature and promotes complete oxidation over C-O coupling. The transition metal site (Fe, Mn) was redox-active, leading to the formation of OCH_3 groups whose coverage increases with transition metal content, indicating that the transition metal sites are active for the MOR. By comparison, the basic O^{2-} sites formed adsorbed CO_3 species with roughly comparable coverages across samples and conditions, present at roughly half the concentration of OCH_3 groups. Oxygen vacancy formation is supported by slight reductions in Fe valence (though remaining primarily +3) with increase in methanol partial pressure for the AMO films. These findings illustrate the nature of active sites for the MOR on AMO films and suggest dispersion of transition metals within an amorphous matrix offers new handles to tailor activity and selectivity in oxidation reactions.

Acknowledgements:

Acknowledgment is made to the donors of The American Chemical Society Petroleum Research Fund for partial support of this work. K.A.S. acknowledges support from Oregon State University as a Callahan Faculty Scholar. Film deposition was supported by the NSF CCI, The Center for Sustainable Materials Chemistry (CHE-1606982). This research used resources of the Advanced Light Source, which is a DOE Office of Science User Facility under contract no. DE-AC02-05CH11231.

394

395 **References**

396 1. G. Iaquaniello, G. Centi, A. Salladini and E. Palo, in *Methanol*, eds. A. Basile and F. Dalena,
397 Elsevier, 2018, DOI: https://doi.org/10.1016/B978-0-444-63903-5.00022-4, pp. 595-612.
398 2. W.-C. Liu, J. Baek and G. A. Somorjai, *Topics in Catalysis*, 2018, **61**, 530-541.
399 3. J. M. Tatibouët, *Applied Catalysis A: General*, 1997, **148**, 213-252.
400 4. M. Badlani and I. E. Wachs, *Catalysis Letters*, 2001, **75**, 137-149.
401 5. L. J. Burcham, L. E. Briand and I. E. Wachs, *Langmuir*, 2001, **17**, 6164-6174.
402 6. H. Bluhm, M. Hävecker, A. Knop-Gericke, E. Kleimenov, R. Schlögl, D. Teschner, V. I. Bukhtiyarov,
403 D. F. Ogletree and M. Salmeron, *The Journal of Physical Chemistry B*, 2004, **108**, 14340-14347.
404 7. M. Bowker, E. K. Gibson, I. P. Silverwood and C. Brookes, *Faraday Discussions*, 2016, **188**, 387-
405 398.
406 8. J. Döbler, M. Pritzsche and J. Sauer, *Journal of the American Chemical Society*, 2005, **127**, 10861-
407 10868.
408 9. H. Hu and I. E. Wachs, *The Journal of Physical Chemistry*, 1995, **99**, 10911-10922.
409 10. K. Kähler, M. C. Holz, M. Rohe, A. C. van Veen and M. Muhler, *Journal of Catalysis*, 2013, **299**,
410 162-170.
411 11. T. Kropp, J. Paier and J. Sauer, *Journal of the American Chemical Society*, 2014, **136**, 14616-
412 14625.
413 12. S. Oh, Y. K. Kim, C. H. Jung, W. H. Doh and J. Y. Park, *Chemical Communications*, 2018, **54**, 8174-
414 8177.
415 13. x. Zhang, X. Chen, Y. Liu and M. Guo, *Water, Air, & Soil Pollution*, 2020, **231**, 277.
416 14. U. S. Ozkan, R. F. Kueller and E. Moctezuma, *Industrial & Engineering Chemistry Research*, 1990,
417 **29**, 1136-1142.
418 15. H.-J. Freund and G. Pacchioni, *Chemical Society Reviews*, 2008, **37**, 2224-2242.
419 16. B. R. Goldsmith, B. Peters, J. K. Johnson, B. C. Gates and S. L. Scott, *ACS Catalysis*, 2017, **7**, 7543-
420 7557.
421 17. M. G. Kast, E. A. Cochran, L. J. Enman, G. Mitchson, J. Ditto, C. Siefe, P. N. Plassmeyer, A. L.
422 Greenaway, D. C. Johnson, C. J. Page and S. W. Boettcher, *Journal of the American Chemical*
423 *Society*, 2016, **138**, 16800-16808.
424 18. M. Aykol and K. A. Persson, *ACS Applied Materials & Interfaces*, 2018, **10**, 3039-3045.
425 19. C. Zhang, R. D. Fagan, R. D. L. Smith, S. A. Moore, C. P. Berlinguette and S. Trudel, *Journal of*
426 *Materials Chemistry A*, 2015, **3**, 756-761.
427 20. L. J. Enman, M. G. Kast, E. A. Cochran, E. Pledger, M. B. Stevens and S. W. Boettcher, *The Journal*
428 *of Physical Chemistry C*, 2018, **122**, 13691-13704.
429 21. K. A. Stoerzinger, L. J. Enman, E. A. Cochran, J. T. Diulus, R. T. Frederick, K. Artyushkova, E. J.
430 Crumlin, G. S. Herman and S. W. Boettcher, *The Journal of Physical Chemistry C*, 2019, **123**,
431 27048-27054.
432 22. M. E. Grass, P. G. Karlsson, F. Aksoy, M. Lundqvist, B. Wannberg, B. S. Mun, Z. Hussain and Z. Liu,
433 *Review of Scientific Instruments*, 2010, **81**, 053106.
434 23. A. Akkerman, T. Boutboul, A. Breskin, R. Chechik, A. Gibrekhterman and Y. Lifshitz, *physica*
435 *status solidi (b)*, 1996, **198**, 769-784.
436 24. E. R. Mysak, J. D. Smith, P. D. Ashby, J. T. Newberg, K. R. Wilson and H. Bluhm, *Physical*
437 *Chemistry Chemical Physics*, 2011, **13**, 7554-7564.
438 25. A. S. Duke, R. P. Galhenage, S. A. Tenney, S. C. Ammal, A. Heyden, P. Sutter and D. A. Chen, *The*
439 *Journal of Physical Chemistry C*, 2015, **119**, 23082-23093.

26. C. Cao and K. L. Hohn, *Applied Catalysis A: General*, 2009, **354**, 26-32.
27. D. J. Miller, M. C. Biesinger and N. S. McIntyre, *Surface and Interface Analysis*, 2002, **33**, 299-305.
28. E. McCafferty and J. P. Wightman, *Surface and Interface Analysis*, 1998, **26**, 549-564.